

An intermetallic powder-in-tube approach to increased flux-pinning in Nb₃Sn by internal oxidation of Zr

L R Motowidlo^{1,4}, P J Lee^{2,5} , C Tarantini² , S Balachandran² ,
A K Ghosh³ and D C Larbalestier² 

¹ Formerly SupraMagnetics Inc., Plantsville, CT 06479, United States of America

² The Applied Superconductivity Center, National High Magnetic Field Laboratory, Florida State University, Tallahassee, FL 32310, United States of America

³ Retired, formerly Brookhaven National Laboratory, Upton, NY 11973, United States of America

E-mail: lee@asc.magnet.fsu.edu, tarantini@asc.magnet.fsu.edu, shreyasb@asc.magnet.fsu.edu, akghosh_11786@yahoo.com and larbalestier@asc.magnet.fsu.edu

Received 25 September 2017, revised 1 November 2017

Accepted for publication 3 November 2017

Published 28 November 2017



Abstract

We report on the development of multifilamentary Nb₃Sn superconductors by a versatile powder-in-tube technique (PIT) that demonstrates a simple pathway to a strand with a higher density of flux-pinning sites that has the potential to increase critical current density beyond present levels. The approach uses internal oxidation of Zr-alloyed Nb tubes to produce Zr oxide particles within the Nb₃Sn layer that act as a dispersion of artificial pinning centres (APCs). In this design, SnO₂ powder is mixed with Cu₅Sn₄ powder within the PIT core that supplies the Sn for the A15 reaction with Nb1Zr filament tubes. Initial results show an average grain size of ~38 nm in the A15 layer, compared to the 90–130 nm of typical APC-free high-*J_c* strands made by conventional PIT or Internal Sn processing. There is a shift in the peak of the pinning force curve from *H*/*H_{irr}* of ~0.2 to ~0.3 and the pinning force curves can be deconvoluted into grain boundary and point-pinning components, the point-pinning contribution dominating for the APC Nb-1wt%Zr strands.

Keywords: Nb₃Sn, powder-in-tube, artificial pinning centres, critical current density, superconducting wire

(Some figures may appear in colour only in the online journal)

1. Introduction

Multifilamentary Nb₃Sn strands have a high manufacturing maturity with very large quantities of low hysteresis loss wires produced for the ITER project (600 t) [1] and high current density strands being procured for the High Luminosity (HiLumi) upgrade to the large hadron collider (4.8 t MQXF) [2, 3]. For applications that require magnetic fields above 15 T, HTS conductors like Bi-2212 can outperform

Nb₃Sn [4] but their cost is still prohibitive for future large scale applications such as the high energy LHC [5] or the future circular collider [6] both of which envision ~16 T dipole operation [7]. However, there are significant challenges to developing Nb₃Sn for practical use in an accelerator at such high fields because the critical current density, *J_c*, target specification of 2300 A mm⁻² (1.9 K, 16 T) or 1500 A mm⁻² at 16 T, 4.2 K [8] is ~50% higher than that of the present HiLumi procurement [9], which is the highest field and highest *J_c* accelerator application so far. Improvements in conductor performance are required to provide operating margin, but any performance increase that can lead to a reduction in cost is also highly desirable because the FCC conductor as currently specified is estimated to represent 50%

⁴ Leszek Motowidlo unexpectedly passed away on 21, September 2016, this paper brings together the available data on the powder-in-tube APC Nb₃Sn strand that he had developed.

⁵ Author to whom any correspondence should be addressed.

Table 1. Summary of PIT wires tested at BNL with heat treatment (HT) conditions.

BNL run	HT temp, °C	HT time, h	Cu/non-Cu ratio	Filaments	Filament diameter, μm	Billet ID	SnO ₂ :Cu ₅ Sn ₄ and comments	Wire dia., mm
3991	625	300	1.0	120	59	APC 550	SnO ₂ ('S')	0.91
3993	650	200	1.0	120	59	APC 550	SnO ₂ ('S')	0.91
3994	650	200	1.0	120	59	APC 550	SnO ₂ ('S')	0.91
4051	632	200	1.0	120	51	APC 555	500 °C/24 h+HT, SnO ₂ ('H')	0.79
4133	630	100	1.0	120	59	APC 555	SnO ₂ ('H')	0.91

of the magnet cost [7]. Although recent developments in the understanding and optimisation of Nb₃Sn strand heat treatments (HTs) have suggested room to improve the critical current density in existing internal Sn [10] and PIT [11] conductors, achieving the FCC specification is a challenge that almost certainly requires enhanced vortex pinning too.

In conventional Nb₃Sn conductors, vortex pinning strength is determined by the grain boundary (GB) density [12]. However, a typical grain diameter of ~ 100 nm is much greater than the ~ 12 nm fluxoid spacing at 16 T, making the pinning efficiency low. Consequently, there have been a number of attempts to introduce additional pinning sites including the powder metallurgical incorporation of Ta ribbons [13, 14], Cu [15, 16], Ag [17], and films doped with Ti or Y [18] and Y, Sc, Dy, Al₂O₃, or Ti [19]. However, none of these attempts has been developed into a successful multifilamentary wire. Internal oxidation of Zr-doped Nb was successfully developed for tapes at general electric (GE) [20]. In the GE tape process, liquid Sn was reacted with Nb foil above 900 °C but the tape critical current density was limited by the resulting large grain size. Doping the Nb tape with Zr and oxygen reduced the A15 grain size to approximately 50 nm (which is \sim half that of modern solid-state reactions). Their TEM studies showed that this process produced coherent ZrO₂ precipitates throughout the Nb₃Sn grains. They also concluded that the slow coarsening of the Nb₃Sn grain size was a result of ZrO₂ precipitates dissolving in shrinking grains and then re-precipitating at the grain boundaries of growing A15 grains. Zeitlin *et al* [21] attempted to adapt this approach to conventional filamentary internal Sn Nb₃Sn wires by adding SnO₂ to the Sn core of Nb-1wt%Zr (Nb1Zr) filament tubes and they did produce some grain refinement at high temperatures. Further progress was made when Xu *et al* [22] concluded that the attempts to adapt the GE technique to internal Sn wires had not been successful because the Cu matrix around each filament had less affinity for oxygen than the Sn and thus had prevented oxygen diffusion into the Nb1Zr. Using a Sn-in-Tube architecture Xu *et al* inserted a SnO₂ layer between the Cu sleeve that normally surrounds the Sn–Cu core and the Nb1Zr matrix and were able to refine the Nb₃Sn grain size to as small as 43 nm. However, scale-up of this approach is challenging because of the required oxide layer between the sleeve and tube. In this paper we demonstrate a potential simplification of this fabrication complexity with a Powder-in-Tube process in which powder mixtures of Cu₅Sn₄ and SnO₂ are inserted into Nb1Zr tubes. We show

that this design provides a flexible alternative artificial pinning centre (APC) vehicle for nano-precipitation of ZrO₂ in the A15 layer.

2. Methods

2.1. Wire Fabrication

Cu₅Sn₄ (η phase) was used as the Sn powder source rather than the NbSn₂ powder of the conventional ECN PIT design [23] because it is less costly and easier to make [24] (the Nb in the NbSn₂ does not contribute to the small-grain A15 phase, whereas the Cu in the Cu₅Sn₄ is required for the low temperature formation of Nb₃Sn). The Cu₅Sn₄ is made by mixing Sn and Cu powders with a starting composition of 59.9 wt% Sn (an atomic ratio of Cu₅Sn₄ [25] and heat-treating them below 400 °C. A significant difference between NbSn₂-based PIT designs and this approach is that the η phase melts at 415 °C, well below the HT temperatures used for Nb₃Sn formation. The Cu₅Sn₄ intermetallic is ball milled and then jet milled to a particle size that was typically 99% $< 3 \mu\text{m}$ (top size of $6 \mu\text{m}$), so that the maximum particle size is significantly smaller than the ultimate filament core size to maintain composite stability during wire drawing. SnO₂ powder mixed with the Cu₅Sn₄ supplies the oxygen. For the composites supplied to BNL, two ratios of SnO₂:Cu₅Sn₄ were used, denoted 'H' and 'S', with the SnO₂ content in mixture 'H' almost double that in 'S'. Wires with undisclosed SnO₂:Cu₅Sn₄ ratios were supplied to FSU and are described as compositions 'SnO₂2X', 'SnO₂1X' and '10SnO₂' to distinguish them from the BNL billet compositions. The mixed powder was packed into Cu-clad Nb-1wt%Zr tubes, which were then drawn to a restack size. Two multifilamentary composite designs were fabricated from these monocoresh; a 7-filament hexagonal stack (figure 1(a)) and a 120 filament octagonal assembly (figure 1(b) that was largely studied at BNL) that allows for the introduction of interfilamentary strengthening elements [24]. The assembled multifilamentary composites were drawn to final diameters ranging from 1 to 0.5 mm. The strands supplied to BNL are summarised in table 1.

2.2. Metallography

Short lengths of heat treated wires were provided by Supra-Magnetics for microstructural and microchemical evaluation. The samples were polished in transverse cross-section and

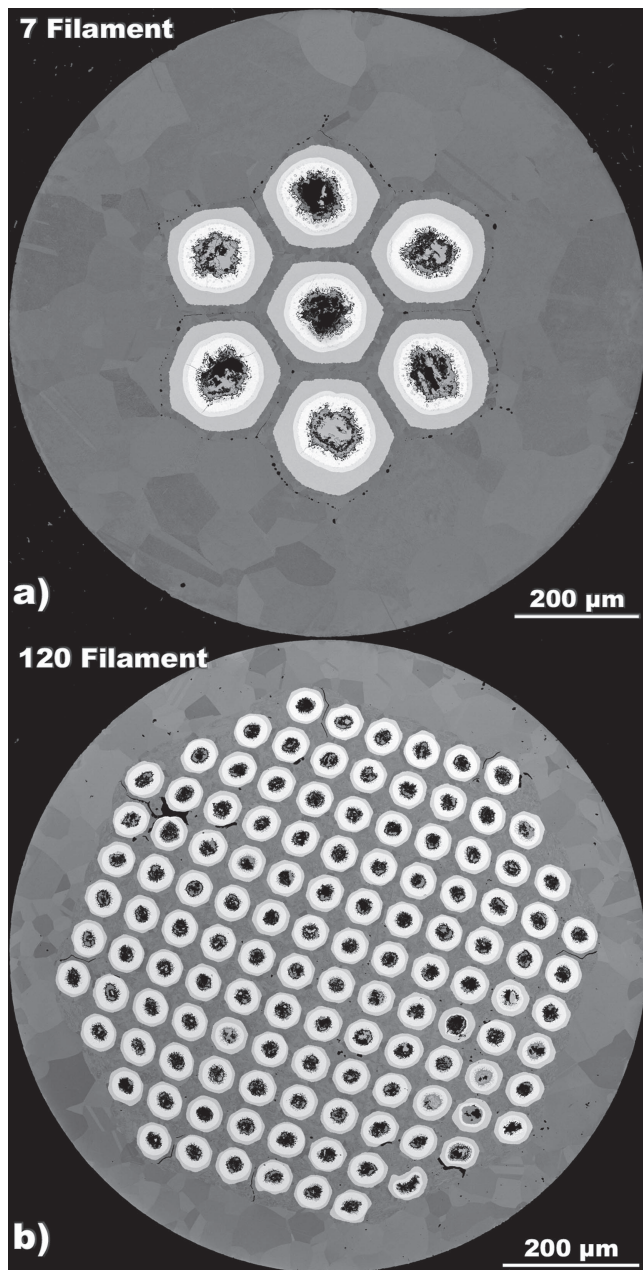


Figure 1. FESEM-BSE images of (a) the reacted 7-filament (300 h/625 °C) and reacted 120 filament (200 h/640 °C) PIT composites.

imaged using a Zeiss 1540EsB CrossBeam field emission scanning electron microscope (FESEM). Microchemical analysis was performed in the FESEM using an EDAX Apollo XP SDD detector energy dispersive x-ray detector.

2.3. Magnetisation Measurements

Magnetisation measurements were performed on the short samples (~5 mm) using a 14 T Oxford Instruments dedicated vibrating sample magnetometer (VSM) capable of operation at variable temperatures from 2 K to above T_c . The critical current density was estimated by the Bean model and the pinning force and Kramer curves were analysed similarly to the transport data (see ahead).

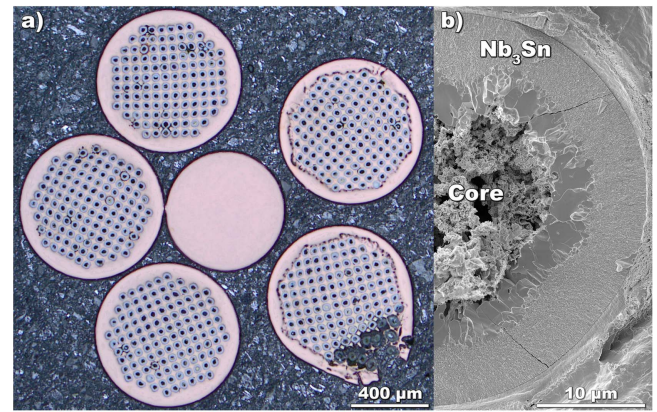


Figure 2. (a) Light microscope image of five transverse cross-sections from a 0.7 mm diameter 120 filament Nb1Zr + SnO₂ sample after a 200 h/650 °C heat treatment. These cross-sections showing Sn leakage and Sn burst are typical of the drawing issues experienced with these strands. (b) FESEM-in-lens secondary electron image of a good filament from the same strand fractured to show the grain size. The small-grain Nb₃Sn layer is labelled.

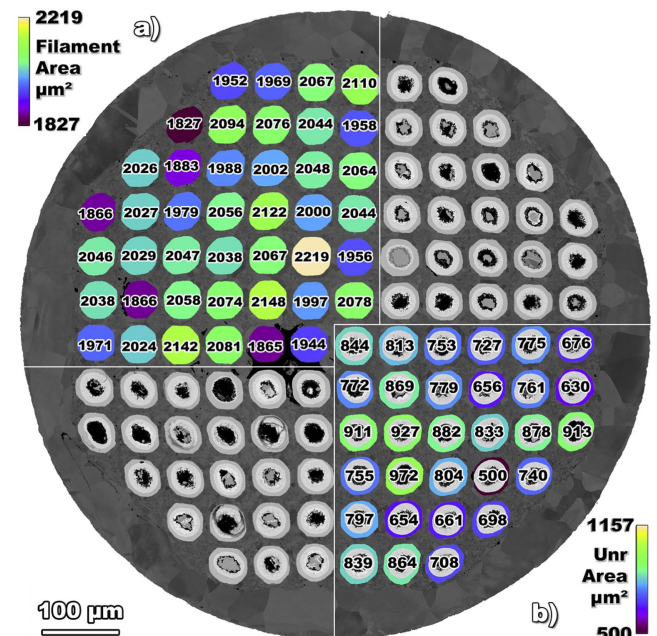


Figure 3. FESEM-BSE image of a 120 filament Nb1Zr + 10SnO₂ sample after a 24 h/500 °C + 200 h/650 °C two-step heat treatment overlaid with quantitative analyses of the filament cross-sections. The top left quadrant analysis (a) indicates total area measurements of the filaments, whereas the bottom right quadrant analysis (b) indicates the residual Nb1Zr filament tube areas after the A15 reaction. The significant variation of unreacted tube-cross-sectional areas is an indicator of pre-existing tube non-uniformities after drawing and prior to reaction.

2.4. Transport Measurements

Unreacted 120 filament wires were supplied to BNL for barrel HT and measurement at magnetic fields up to 15 T. The ramp up to the HT reaction temperature was typically at a rate of 25 °C h⁻¹. Transport measurement was on a standard ITER with the central 7 turns in a uniform field, using the

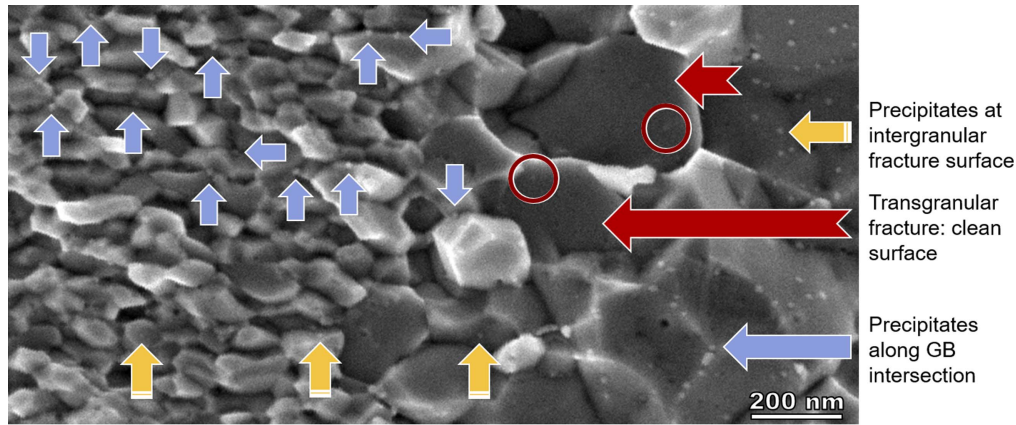


Figure 4. FESEM-in-lens secondary electron image of fracture surface at the interface between the large and small-grain regions in a representative region of a 120 filament Nb1Zr + '10SnO₂' sample after a 300 h/630 °C heat treatment. Precipitate-like features that we assume to be ZrO₂ are most commonly observed at grain boundary intersections (blue arrows) and less commonly at intergranular surfaces (orange arrows). For fractures through the grains (red arrows) there were no surface features but occasionally faint precipitate-scale contrast (red circles) that might indicate fracture through interior precipitates.

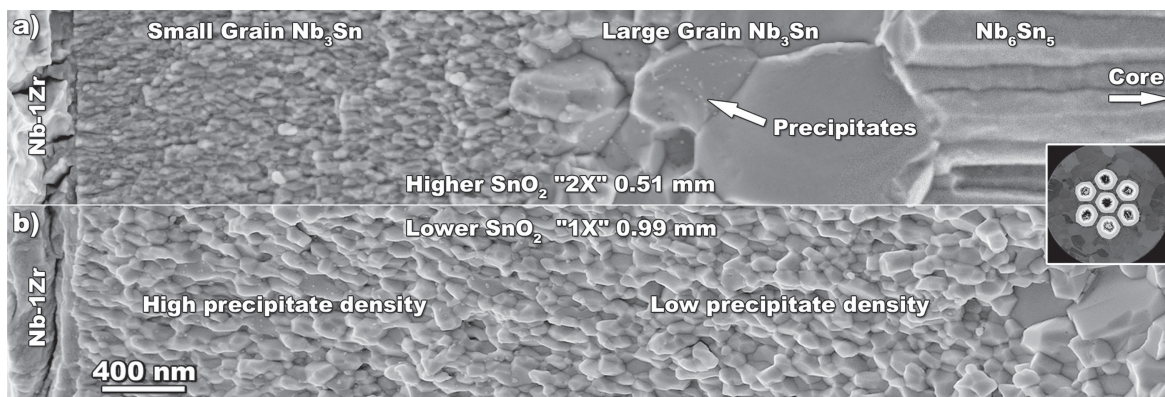


Figure 5. FESEM-in-lens secondary electron images of fracture surfaces of the small-grain Nb₃Sn layers in two 7-filament (inset) composites with different Cu₅Sn₄:SnO₂ ratios. Both samples were heat treated at 625 °C for 300 h, (a) is at a wire diameter of 0.51 mm with higher ratio 'SnO₂2X' and (b) at 0.99 mm diameter with lower ratio 'SnO₂1X'. The higher SnO₂:Cu₅Sn₄ ratio produced an A15 grain diameter that was ~ half the lower ratio 'SnO₂1X' sample. We did not observe precipitate contrast in the transgranular fractures.

0.1 $\mu\text{V cm}^{-1}$ criterion and a measured sample length of 0.7 m. The data were analysed by fitting the volume flux-pinning curve $F_p(H)$ (with self-field correction) to the generic expression $F_p(H) = C \cdot h^p (1 - h)^q$, where C is a constant, $h = H/H_{\text{irr}}$, and H_{irr} is the irreversibility field. Standard process Nb₃Sn conductors without point pins are generally fit well by $p = 0.5$ and $q = 2.0$, which is essentially the Kramer fit [26] with B_{c2} being appropriately replaced by the Kramer field H_K extrapolation from ~10 to 15 T to define the irreversibility field at which J_c becomes zero.

3. Results

3.1. Microstructures

3.1.1. General observations. The multifilament wires were difficult to draw to final size without breakage and even unbroken wires had broken filaments. In figure 2(a) we show five cross-sections from the same ~50 mm length of a 120

filament composite after a reaction heat treatment of 200 h at 650 °C. A significant number of filament tubes have been breached and in one case there was Sn burst to the outside. Nevertheless, as shown in figure 2(b), an extensive small-grain Nb₃Sn layer was found after reaction in the unbreached filaments of this strand.

The difficulty in drawing the composites to final size was attributed to a difficulty in obtaining Nb1Zr tube of the correct size and quality. Figure 3, is a cross-sectional BSE image of a 120 filament Nb1Zr + SnO₂ sample after a 24 h/500 °C + 200 h/650 °C two-step heat treatment that we have colour-coded to contrast the total filament areas with the residual Nb1Zr areas after the A15 reaction. The quantitative image analysis indicated that the overall filament cross-sectional areas (as indicated in figure 3(a)) were fairly uniform, between 1800 and 2200 μm^2 . The residual unreacted Nb1Zr areas were much more variable, with the unreacted areas differing by almost a factor of 2 from 500 μm^2 to 1100 μm^2 . This large disparity is one indication of non-uniform deformation, and thinning of the Nb1Zr tubes

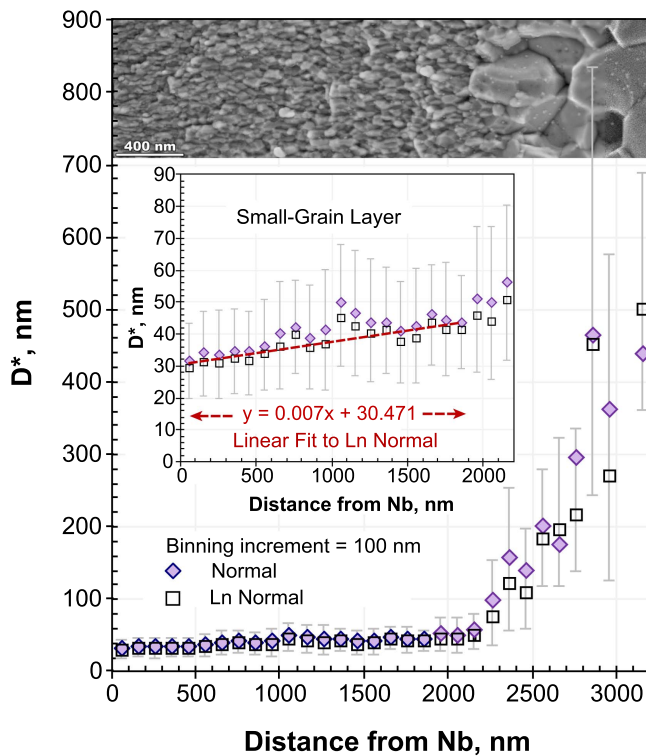


Figure 6. Area equivalent grain diameter variation with distance from the unreacted Nb1Zr interface for the high $\text{SnO}_2\text{:Cu}_5\text{Sn}_4$ composition ‘ $\text{SnO}_2\text{2X}$ ’ 7-filament strand in figure 5(a). The size distribution is log-normal but both log-normal and normal averages for each bin are applied for comparison with other published data. The least-squares linear fit is applied to the log-normal data across the small grain range indicated. Error bars show \pm one sample standard deviation based on log-normal statistics for each bin.

during drawing as well as local variation induced by Sn loss from locally thinned and broken tube walls.

The samples were fractured to reveal the grain size as Nb_3Sn typically fractures along the grain boundaries. On these GB fracture surfaces, we observed precipitate-like features similar in size and distribution to those observed by Xu *et al* using TEM [27]. These features, assumed to be ZrO_2 precipitates, ranged in size from 5 to 15 nm in diameter but they were too small to confirm as ZrO_2 by compositional analysis in the FESEM. The oxidation of Zr is thermodynamically favoured over Nb, Sn and Cu and Rumaner *et al* found by electron diffraction in TEM that the precipitates in their Nb-1Zr experiments (by a quite different approach and using high temperatures where the Zr is more mobile) were monoclinic ZrO_2 [20]. We did not observe particles in fractured surfaces in a Ta-doped PIT sample using the same Cu_5Sn_4 powder but no SnO_2 or Zr [25], however, fracture performed elsewhere of Nb_3Sn that was not designed for oxidation has produced surface particulates of similar size and contrast [28, 29]. An example of the precipitates at the interface between the large and small-grain A15 regions is shown in figure 4. The precipitates are sparsely distributed with rarely more than one precipitate per GB segment in the small-grain regions. Most commonly, the precipitates are observed at GB intersections (some examples are indicated by

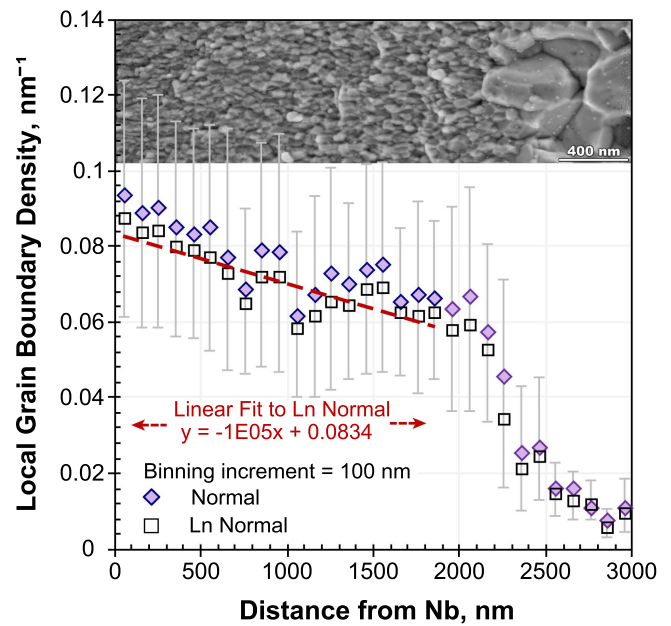


Figure 7. Decrease of Nb_3Sn grain boundary density with increasing distance from the reaction front at the Nb1Zr interface for the high $\text{SnO}_2\text{:Cu}_5\text{Sn}_4$ composition ‘ $\text{SnO}_2\text{2X}$ ’ 7-filament strand in figure 5(a). The size distribution is log-normal but the mean of both log-normal and normal for each bin are presented. The least-squares fit is applied to the log-normal data across the small grain size range indicated. Error bars show \pm one sample standard deviation based on log-normal statistics for each bin.

the blue arrows in figure 4). Less frequently, the precipitates are observed at GB surfaces (as indicated by the orange arrows in figure 4). In figure 4 we also show some large grains (red notched arrows) that have fractured through the grains rather than at the grain boundaries, and in these we see no surface precipitates. There is, however, some faint contrast on the scale of the ZrO_2 precipitates that might suggest that the fracture has sliced through precipitates.

3.1.2. $\text{Cu}_5\text{Sn}_4\text{:SnO}_2$ ratio. In figure 5 fracture surfaces from two 7-filament composites with different $\text{Cu}_5\text{Sn}_4\text{:SnO}_2$ ratios but the same heat treatment (300 h/625 °C) are contrasted. Composition ‘ $\text{SnO}_2\text{2X}$ ’ (figure 5(a)), is higher in SnO_2 and produces a much finer (<30 nm diameter near the Nb1Zr interface) A15 grain size than composition ‘ $\text{SnO}_2\text{1X}$ ’ (figure 5(b)). However, there is a clear grain size gradient with the grain diameter becoming smaller towards the Nb1Zr interface (outer edge of reaction front). However, the small-grain layer is \sim half the thickness for lower SnO_2 ‘ $\text{SnO}_2\text{1X}$ ’ strand. This might be related to the smaller strand diameter (0.51 mm compared with 0.91 mm) or that the reaction is proceeding slower. The precipitates also appear to be smaller for the higher SnO_2 ratio sample. All the samples had an interior layer of much larger A15 grains, as is found for conventional PIT Nb_3Sn wire. As indicated in figure 5(b), closer to the core in the low- SnO_2 sample, the precipitate density is greatly reduced, suggesting a depleted oxygen supply in the low- SnO_2 sample and inability to convert all the Zr to ZrO_2 . The area-equivalent A15 grain diameter for the

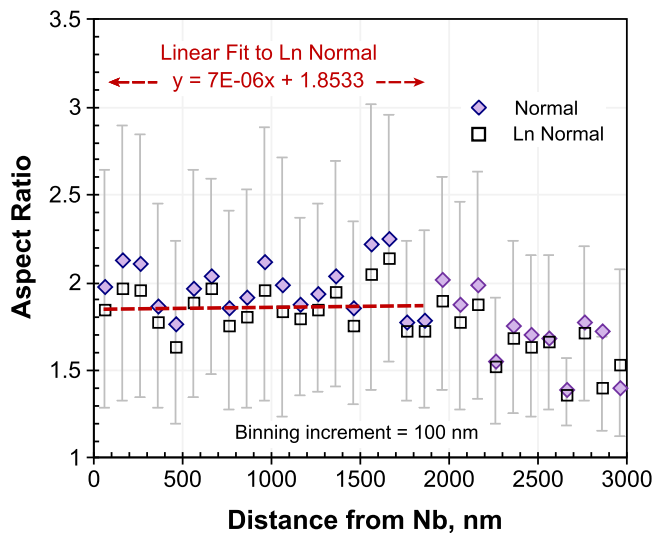


Figure 8. The aspect ratios for the Nb_3Sn grains as a function of distance from the unreacted Nb1Zr interface for the high $\text{SnO}_2\text{:Cu}_5\text{Sn}_4$ composition ‘ $\text{SnO}_2\text{2X}$ ’ 7-filament strand in figure 5(a). The least-squares fit indicates that the aspect ratio is remarkably uniform across the small-grain A15 layer. The least-squares fit is applied to the log-normal data across the small grain range indicated. Error bars show \pm one sample standard deviation based on log-normal statistics for each bin.

low- SnO_2 sample increased from ~ 77 nm at the Nb-1Zr interface to ~ 86 nm at the small-grain:large-grain interface. Both samples have a thick Nb_6Sn_5 layer adjacent to the large-grain Nb_3Sn layer. This thick interior layer of Nb_6Sn_5 is effectively a trapped Sn supply because bulk diffusion of Sn through Nb_3Sn is orders of magnitude slower than along grain boundaries [11, 37] and the large grains offer sparse outward diffusion paths for the Sn. Note that, unlike conventional PIT Nb_3Sn which uses NbSn_2 powder in the core as the Sn source, in this SupraMagnetics Cu_5Sn_4 core design all the Nb for the Nb_3Sn and Nb_6Sn_5 phases is supplied by the Nb1Zr tube.

In these 7-filament composites the small-grain Nb_3Sn area was only 7.1% of the filament cross-section for the sample in figures 5(a) and 9.9% for the sample in figure 5(b) compared with $\sim 40\%$ of the cross-section for fully optimised accelerator quality PIT Nb_3Sn strands [11, 31].

3.1.3. Microstructural gradients The A15 grain size gradient in figure 5(a) is quantified in figure 6 in terms of area equivalent grain diameter (the diameter calculated from the cross-section area assuming a circular cross-section). The A15 grain diameter is as small as 30 nm near the unreacted Nb1Zr interface and rises to a little over 40 nm near the original growth front neighbouring the large-grain region. The error bars show the log-normal standard deviations. Both values are much smaller than the ~ 90 – 150 nm size in conventional Zr-free A15 wires.

The impact on vortex pinning should be clearer when plotted in terms of GB density, as is shown in figure 7, which increases by about 40% towards the outer edge of the reaction front. Because the grain size of the last A15 to form is smaller than that at the original core/ Nb1Zr interface, it appears that

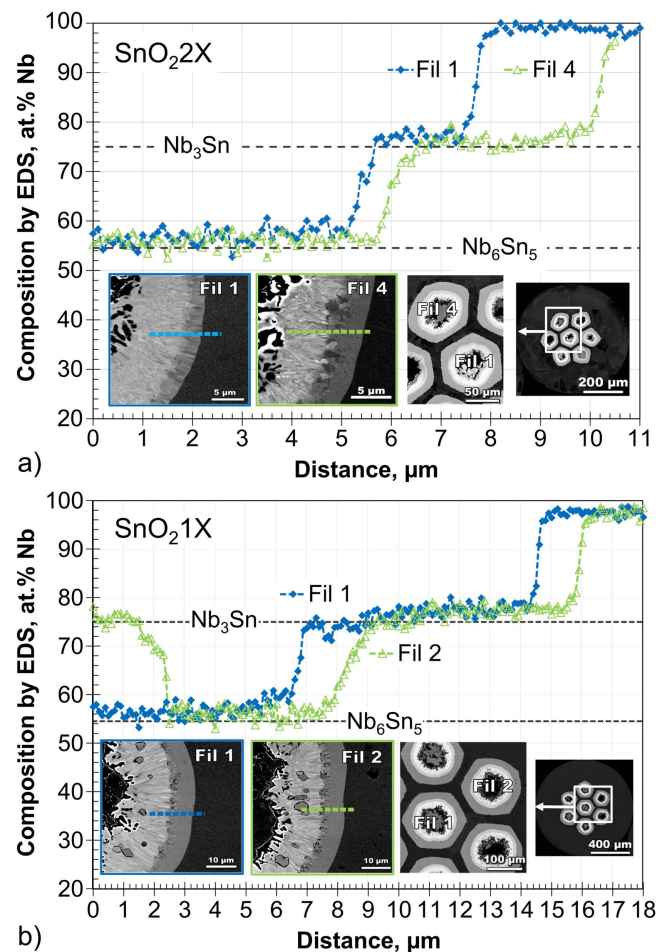


Figure 9. EDS analysis of 7-filament Zr/ SnO_2 with (a) $\text{Cu}_5\text{Sn}_4\text{:SnO}_2$ ratio ‘ $\text{SnO}_2\text{2X}$ ’ (strand in figure 5(a)) and (b) ‘ $\text{SnO}_2\text{1X}$ ’ (strand in figure 5(b)), both heat treated for 300 h/625 °C. In (a) the thicker ‘Fil 4’ Nb_3Sn layer has a composition that is closer to stoichiometry than the central ‘Fil 1’, suggesting some Sn loss from this filament. In (b) the Nb_6Sn_5 layer contains some large Nb_3Sn grains 1–3 μm in diameter.

some grain growth occurs as the A15 reaction front penetrates into the tube.

In figure 8 we plot the Nb_3Sn grain aspect ratio against distance from the Nb1Zr tube interface. We find a very constant aspect ratio across the fine grain region. A low Sn content as occurs at the Nb-A15 interface is often associated with an increase in A15 grain aspect ratio so this result is consistent with the uniform compositions reported in figures 9(a) and (b). The ZrO_2 precipitates may, however, also play a role in nucleating new A15 grains and in this way inhibit columnar growth.

3.1.4. Microchemical analysis. EDS analyses of filament layers from the $\text{SnO}_2\text{2X}$, and $\text{SnO}_2\text{1X}$ samples shown in figure 5 are shown in figures 9(a) and (b) respectively. The composition of Nb_3Sn produced during the final reaction heat treatment is close to stoichiometric across most of the Nb_3Sn layer for Filament 4 in figure 9(a) ($\text{SnO}_2\text{2X}$) but is Sn-poor for the thinner A15 layer in the central filament (Filament 1) suggesting that there has been Sn loss through the tube to the

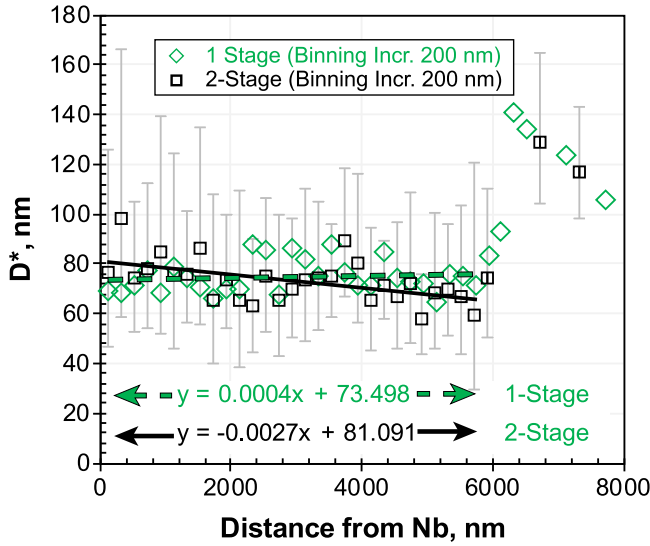


Figure 10. Area equivalent grain diameter (ln-normal) variation with distance from the unreacted Nb-1Zr interface for a 120 filament Nb1Zr + 10SnO₂ composite heat treated with a single 300 h/630 °C heat treatment (green) and a dual-stage HT of 200 h/625 °C + 100 h/650 °C (black). The grain size is similar at the centre of the layer (<80 nm) but the 2-stage heat treatment produces an A15 grain size gradient across the layer. Least-square linear fits are shown for the data across the small-grain layers.

surrounding Cu in this filament. The Sn composition for Filament 4 of the SnO₂2X wire eventually declines over the outer ~1 μm of the small-grain layer.

For the SnO₂1X sample, both filaments shown in figure 9(b) have a composition gradient across the A15 layer. An interesting observation is that there are large Nb₃Sn grains that occur deep inside the Nb₆Sn₅ layer in filaments with the lower SnO₂ composition ‘SnO₂1X’ wire, as is seen in figure 9(b). For conventional PIT made with NbSn₂ powder precursor, Nb₆Sn₅ is an intermediate reaction phase that forms adjacent to the Nb tube during A15 layer growth and invariably decomposes to large-grain A15 by loss of Sn to the growing small-grain Nb₃Sn layer. The fact that a residual Nb₆Sn₅ layer is found at the interface indicates imperfect Sn diffusion into the filament tube that could have enabled further small-grain A15 layer growth.

3.1.5. Two-stage reaction heat treatment. In figure 10 we compare the Nb₃Sn area-equivalent grain diameters of the same 120 filament Nb1Zr + 10SnO₂ composite heat treated with a single HT of 300 h at 630 °C with a dual-stage HT (200 h/625 °C + 100 h/650 °C) starting at a lower and finishing at a higher temperature. The dual-stage heat treatment with a final stage at 650 °C did not greatly coarsen the grain size as compared to the single HT (the average grain size of <80 nm for both strands is small for PIT Nb₃Sn) as is usually the case for Zr-free wires. The rationale for the second, higher temperature 650 °C step is to drive more compositional uniformity across the A15 layer assuming that it is possible to establish a fine grain size at the lower temperature of the first stage. It seems that this has been quite successful because the initially formed grains

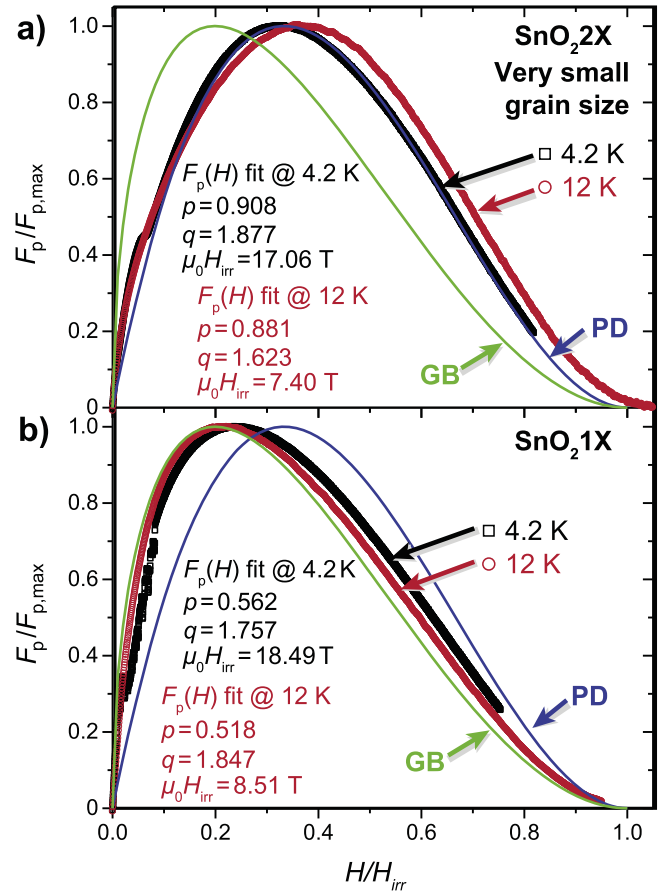


Figure 11. Normalised pinning force curves for (a) composition ‘SnO₂2X’ with small grains and (b) composition ‘SnO₂1X’ with larger grains at 4.2 K and 12 K. The ideal curves for grain boundary GB (green) and point defect PD (blue) pinning are also shown and the fitting parameters are reported.

furthest away from the unreacted Nb1Zr interface are small (~70 nm) and the final grains only slightly larger (~80 nm). This compares with a d^* of ~90 nm for a similarly heat treated (280 h/625 °C) Nb-Ta, Zr-free, PIT strand [11].

3.2. Magnetisation results

Magnetisation measurements at FSU enabled both 4.2 and 12 K properties to be obtained with derivation of the whole F_p curve at 4.2 and 12 K (shown in figure 11) for the samples whose microstructures are shown in figure 5. Higher SnO₂:Cu₅Sn₄ ratio ‘SnO₂2X’ produced a very small Nb₃Sn grain size of ~30–40 nm, and pinning force curves peaking at higher reduced field with a curve shape approaching that expected for point defect (PD) pinning. In contrast, composition ‘SnO₂1X’ produced a curve peaking at lower reduced field that more closely matched that for sparse GB pinning, consistent with its larger grain size. If the precipitates in the ‘SnO₂2X’ sample are also smaller they may be more effective as point pinning sites. However, fitting the pinning force curves with the generic relation $F_p/F_{p,max} \propto (H/H_{irr})^p (1 - H/H_{irr})^q$, $\mu_0 H_{irr}$ (4.2 K) for composition ‘SnO₂2X’ fell to 17.1 T compared with 18.5 T for composition ‘SnO₂1X’.

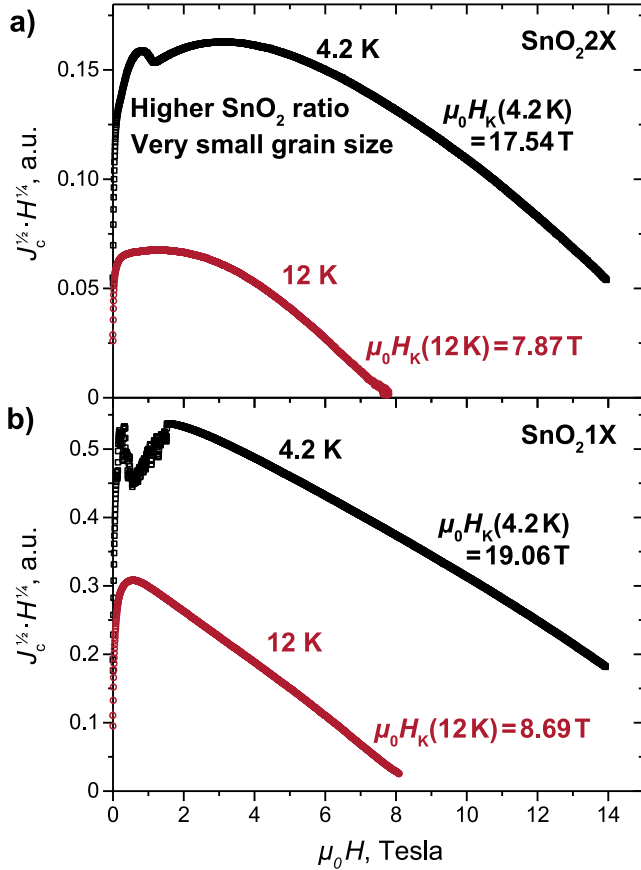


Figure 12. A comparison of the magnetisation-derived Kramer plots for (a) the high SnO_2 : Cu_5Sn_4 composition 'SnO₂2X' wire with smaller grains and (b) composition 'SnO₂1X' wire with larger grains and less ZrO₂ at 4.2 and 12 K. The very small grain size microstructure (a) shows a clear deviation from the usual linearity of Kramer plots for Zr-free Nb₃Sn wires.

Both values are smaller than would be expected from binary Zr-free wires. Also the p and q parameters are close to the values for GB pinning for 'SnO₂1X' and close to the values for PD pinning for 'SnO₂2X'.

Alternatively, using a two-contribution fit (see section 3.3), the relative contributions of PD and GB pinning were 89% PD, for composition 'SnO₂2X', but only 24% for 'SnO₂1X', consistent with the smaller precipitate density of the lower SnO_2 : Cu_5Sn_4 core wire. The estimated small-grain-layer $J_{\text{cm-layer}}$ (4.2 K, 12 T) for the high SnO_2 : Cu_5Sn_4 composition 'SnO₂2X' was $\sim 4500 \text{ A mm}^{-2}$ (a high value for a Zr-free strand compared to our previous highest small-grain layer 12 T J_c value for a binary conventional PIT strand of 3300 A mm^{-2} [30]). For composition 'SnO₂1X' the estimated small-grain-layer $J_{\text{cm-layer}}$ (4.2 K, 12 T) was about 2900 A mm^{-2} , thus showing no advantage.

In figure 12 we compare the magnetisation-derived Kramer plots for the same samples as in figure 11. The Kramer plot should be linear if sparse grain boundaries are the only effective pinning centres. However, we do observe a distinctly nonlinear Kramer plot in the ultra-small-grain sized sample (composition 'SnO₂2X'), which also had a markedly higher layer J_c .

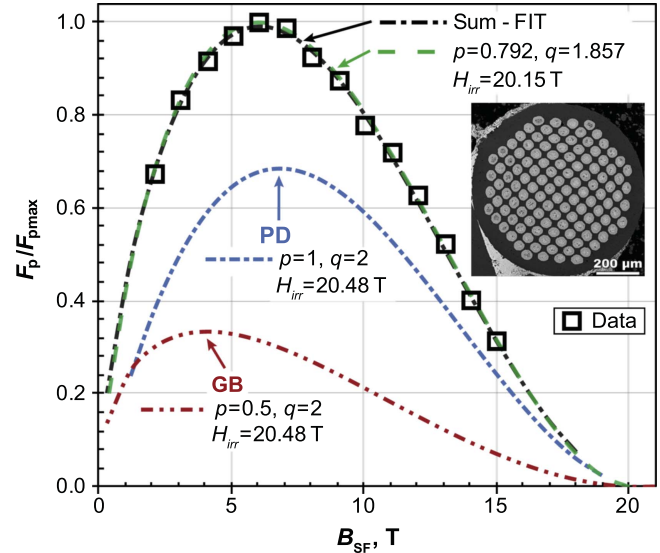


Figure 13. The normalised F_p is plotted as a function of the reduced field for Run # 3991: SnO_2 ('S')+Nb1Zr 300 h@625 °C: 120 Filament APC. The deconvolution into GB and PD pinning components shows that PD pinning dominates with 68% contribution to F_p . H_{irr} is found to be 20.48 T. When the exponents and H_{irr} are allowed to vary, the best fit to the data is shown by the dashed curve, which is very close to the summation curve.

3.3. Transport measurements

Billets L550 and L555 used the 120 filament PIT design with lower and higher SnO_2 ratios respectively. Consistent with the cross-sections, evidence of damage to the filaments appeared in the degraded n -values of ~ 5 . However, even though the transport critical currents are low due to poor filament quality, it was possible to measure their I_c from 15 T to very low fields, and thus determine the normalised flux-pinning curve, $f_p = F_p/F_{p\text{max}}$, as a function of field. Measurements below 2 T are not shown, since they then include an additional contribution from the unreacted Nb.

The I_c measurements were fitted by varying the parameters p and q and B_{c2} . An example is shown in figure 13 where the normalised F_p is plotted as a function of the self-field corrected magnetic field, B_{SF} , for a strand from billet 550 reacted at 625 °C for 300 h. The best overall fit is obtained for $p = 0.792, q = 1.857$ and $B_{c2} = 20.15 \text{ T}$. The non-standard exponents p and q suggest that the pinning is not only from grain boundary pinning ($p = 0.5, q = 2.0$), but also from an additional contribution, as has been observed in enhanced J_c Nb₃Sn wires with radiation-induced PDs within the grains [32]. These additional point pins shift the maximum of the pinning curve from $b = 0.20$ to $b \sim 0.27$. Indeed, we can realistically deconvolute the data set of figure 13 into two components with fixed classical p and q values of $p = 1, q = 2$ for PD pinning and $p = 0.5, q = 2$ for GB pinning, where the PD component dominates the total pinning, especially at higher fields where higher J_c is most desirable.

The analyses of the transport-current-tested strands are summarised in table 2. The best pinning force fits were found for two-component PD + GB pinning for all the APC strands. The PD contribution ranged from 65% to 76%. Billet

Table 2. Summary of J_c and n -values (12 T, 4.22 K, non-self-field corrected) and pinning force fits for PIT wires tested at BNL.

Run no	Billet	HT	J_c (non-Cu A mm ⁻²)	n	p	q	C^a	H_{irr} (T)	Two component fit:	H_{irr} (T)	% PD
3991	550	300 h/625 °C	109	3.3	0.79	1.86	9.44	20.15	PD ($p = 1$) and GB ($p = 0.5$)	20.48	68%
3993	550	200 h/650 °C	162	3.5	0.72	1.42	10.09	18.82	PD ($p = 1$) and GB ($p = 0.5$)	21.08	69%
3994	550	200 h/650 °C	182	3.9	0.80	1.67	13.11	19.74	PD ($p = 1$) and GB ($p = 0.5$)	20.80	76%
4051	555 ^b	48 h/540 °C, 200 h/632 °C	89	2.6	0.78	1.66	5.14	21.79	PD ($p = 1$) and GB ($p = 0.5$)	23.30	71%
4133	555 ^b	10 °C h ⁻¹ + 100 h/630 °C	42	2.6	0.75	1.65	3.06	21.40	PD ($p = 1$) and GB ($p = 0.5$)	22.79	65%

^a Slope of the Kramer plot of F_p (A T mm⁻²) versus $b^p(1 - b)^q$.

^b Higher proportion of SnO₂ powder in the core.

555 had a higher proportion of SnO_2 powder in the core but had similar PD contributions to the other billet. In fact the lowest PD value was obtained from billet 555 strand that was reacted with a slow ramp rate of 10°C h^{-1} from room temperature to 630°C and held there for 100 h to reduce grain growth and thereby increase the GB pinning density. It appears that increasing the SnO_2 powder fraction in this composite does little to enhance the pinning, although the B_{c2} is ~ 2 T higher than that observed for billet 550.

4. Discussion

Despite the poor filament quality arising from low quality Nb1Zr tubes, the results reported here show that the PIT approach with Cu_5Sn_4 and SnO_2 is a viable method to deliver oxygen for the internal oxidation of Zr in Nb. By incorporating Cu as η - Cu_5Sn_4 in the powder core, the Cu can reduce the reaction temperature without blocking oxygen diffusion as was the case with earlier attempts at internal oxidation [21]. Recent work by Xu *et al* [33] has indicated that Nb-Sn intermetallics may still impede oxygen diffusion from the core requiring more SnO_2 and further HT modification to overcome this issue.

Both magnetisation and transport measurements on the SupraMagnetics strands showed that this approach of introducing ZrO_2 precipitates and refining the grain size from 90 nm in Zr-free wires to less than 40 nm shifts the peak in the pinning force curve from about $b \sim 0.2$ to as high as 0.35 in figure 11, as is expected from a large point pinning component. These results are similar to the very small grain size (20–50 nm diameter) films [34] that produced a shift in the peak of $F_p(H)$ to almost $0.4H_{irr}$ in thin films (Nb sputtered onto a bronze substrate and then reacted). Using transport J_c barrel measurements, the F_p curves could be deconvoluted into a dominant PD contribution (65%) to F_p that is similar to the PD irradiation effects observed by Baumgartner *et al* [32]. An even larger 89% PD contribution was estimated by magnetic measurements on the 30–45 nm grain size sample.

For high-field magnet conductor use there is still some uncertainty as to the potential of this approach as there was significant suppression of the Kramer extrapolated fields for all samples. Normally speaking the $\mu_0 H_{c2}$ of binary Nb_3Sn is 23–24 T [35], as compared to the ~ 17.5 –22 T values found here (which are similar to the values of 20.5 and 21.3 T obtained by Xu *et al* for their Nb1Zr APC [22]). The depression was notably larger for the higher SnO_2 7-filament sample with the very small A15 grain size. Whether the degradation of H_{irr} is due to Zr or perhaps to strain induced by ZrO_2 within the A15 grains is not yet clear but this is something that needs verification because a high critical field is essential for reaching high critical currents at fields above 16 T. All modern Nb_3Sn wire use Ta or Ti or a combination of Nb and Ti dopants to increase their high-field performance by increasing H_{c2} [36] and verification of the effectiveness of

ZrO_2 using Nb alloys containing Ti or Ta to enhance the upper critical field will be needed.


5. Conclusions

1. A viable route to an APC (artificial pinning centre) Nb_3Sn has been demonstrated in multifilamentary PIT strand by internal oxidation of Nb1Zr tubes using a core powder mixture of η -phase Cu_5Sn_4 powder and SnO_2 . However, the volume of small-grain Nb_3Sn produced in these demonstration samples was only $\sim 18\%$ – 25% of that for modern accelerator-quality PIT Nb_3Sn , so significant improvements in package efficiency and heat treatment optimisation will be required to make this process competitive.
2. Cu_5Sn_4 does not appear to interfere with the diffusion of oxygen from $\text{SnO}_2/\text{Cu}_5\text{Sn}_4$ powder mixtures into Nb1Zr filament tubes. This suggests that only small modifications to existing internal Sn and PIT approaches will be necessary to fully prove out this method of enhancing vortex pinning in Nb_3Sn , providing that pure Cu does not sit between the Sn and Nb1Zr during the reaction step.
3. A shift in the peak of the pinning force curve to higher reduced fields was similar to that observed for APC thin films and recent radiation experiments. However, as in recent work by Xu *et al* [22], the Kramer fields were significantly depressed from that found in the best Zr-free binary conductors.
4. The pinning force curves can be deconvoluted into contributions from point and GB pinning with point pinning supplying up to 89% of the pinning force for the APC strands in the most favourable case. The estimated Nb_3Sn small-grain layer J_{cm} (12 T, 4.2 K) was $\sim 36\%$ higher than that previously reported for a conventionally processed binary PIT.
5. The applicability of this technique to optimising high-field performance still needs to be demonstrated using alloys incorporating Ti and/or Ta to increase H_{c2} .
6. Better tube quality that maintains its integrity through the drawing cycle so that η phase is not lost when melted and an understanding of why some filaments are left with partial Nb_3Sn reactions and thick Nb_6Sn_5 layers should yield much better critical current values. The issue of microstructural gradients will also have to be addressed.

Acknowledgments

This material is based upon work supported by the US Department of Energy, Office of Science, Office of High Energy Physics under SBIR Program award DE-SC0009605 with additional support from award DE-SC0012083 and the State of Florida. The NHMFL is supported by the NSF under award NSF-DMR-1157490. Jeremiah McCallister provided additional metallographic support.

ORCID iDs

P J Lee  <https://orcid.org/0000-0002-8849-8995>
 C Tarantini  <https://orcid.org/0000-0002-3314-5906>
 S Balachandran  <https://orcid.org/0000-0002-0077-8504>
 D C Larbalestier  <https://orcid.org/0000-0001-7098-7208>

References

- [1] Devred A, Backbier I, Bessette D, Bevilard G, Gardner M, Jong C, Lillaz F, Mitchell N, Romano G and Vostner A 2014 Challenges and status of ITER conductor production *Supercond. Sci. Technol.* **27** 044001
- [2] Bottura L, de Rijk G, Rossi L and Todesco E 2012 Advanced accelerator magnets for upgrading the LHC *IEEE Trans. Appl. Supercond.* **22** 4002008
- [3] Ambrosio G 2015 Nb₃Sn high field magnets for the high luminosity LHC upgrade project *IEEE Trans. Appl. Supercond.* **25** 1–7
- [4] Jiang J, Francis A, Alicea R, Matras M, Kametani F, Trociewitz U P, Hellstrom E E and Larbalestier D C 2017 Effects of filament size on critical current density in overpressure processed Bi-2212 round wire *IEEE Trans. Appl. Supercond.* **27** 1–4
- [5] Rossi L 2016 High-luminosity LHC *Future Research Infrastructures: Challenges and Opportunities (Proc. Int. School of Physics 'Enrico Fermi' vol 194)* pp 61–72
- [6] Tommasini D et al 2017 The 16 T dipole development program for FCC *IEEE Trans. Appl. Supercond.* **27** 1–5
- [7] Schoerling D, Durante M, Lorin C, Martinez T, Ruuskanen J, Salmi T, Sorbi M, Tommasini D and Toral F 2017 Considerations on a cost model for high-field dipole arc magnets for FCC *IEEE Trans. Appl. Supercond.* **27** 1–5
- [8] Ballarino A and Bottura L 2015 Targets for R&D on Nb₃Sn conductor for high energy physics *IEEE Trans. Appl. Supercond.* **25** 1–6
- [9] Cooley L D, Ghosh A K, Dietderich D R and Pong I 2017 Conductor specification and validation for high-luminosity LHC quadrupole magnets *IEEE Trans. Appl. Supercond.* **27** 1–5
- [10] Sanabria C, Lee P J and Larbalestier D C 2017 The vital role of a well-developed Sn-Nb-Cu membrane for high J_c RRP Nb₃Sn wires *unpublished result, presentation STP531 (4Mor2A-04)* <http://snf.ieeeesc.org/snf-issue-no-38-october-2016>
- [11] Tarantini C, Segal C, Sung Z H, Lee P J, Oberli L, Ballarino A, Bottura L and Larbalestier D C 2015 Composition and connectivity variability of the A15 phase in PIT Nb₃Sn wires *Supercond. Sci. Technol.* **28** 095001
- [12] Scanlan R M, Fietz W A and Koch E F 1975 Flux pinning centers in superconducting Nb₃Sn *J. Appl. Phys.* **46** 2244–9
- [13] Gauss S and Flükiger R 1987 Powder metallurgical alternative for the processing of (Nb–Ta)₃Sn multifilamentary wires, starting from elementary Nb and Ta powder *IEEE Trans. Magn.* **23** 657–60
- [14] De Morantville K, Yu D and Wong J 1993 Development of a niobium-tin multifilamentary wire with artificial tantalum inclusions *IEEE Trans. Appl. Supercond.* **3** 982–5
- [15] Kitai T, Higuchi M and Osamura K 1997 Artificial pinning centres in jelly-roll processed NbCu composites *Cryogenics* **37** 389–95
- [16] Rodrigues C A and Rodrigues D 2006 Development and characterization of Nb₃Sn superconductor wire with nanometric-scale pinning centers *J. Phys.: Conf. Ser.* **43** 43–6
- [17] Dietderich D R and Scanlan R M 1995 Characterization of superconductors with artificial pinning microstructures *IEEE Trans. Appl. Supercond.* **5** 1777–80
- [18] Dietderich D R and Scanlan R M 1997 Nb₃Sn artificial pinning microstructures *IEEE Trans. Appl. Supercond.* **7** 1201–4
- [19] Dietderich D R, Kelman M, Litty J R and Scanlan R M 1998 High critical current densities in Nb₃Sn films with engineered microstructures—artificial pinning microstructures *Adv. Cryo. Eng.* **44** 951–8
- [20] Rumaner L E, Benz M G and Hall E L 1994 The role of oxygen and zirconium in the formation and growth of Nb₃Sn grains *Metall. Mater. Trans. A* **25** 213–9
- [21] Zeitlin B A, Gregory E, Marte J, Benz M, Pyon T, Scanlan R and Dietderich D 2005 Results on mono element internal tin Nb₃Sn conductors (MEIT) with Nb7.5Ta and Nb(1Zr + O_x) filaments *IEEE Trans. Appl. Supercond.* **15** 3393–8
- [22] Xu X, Sumption M, Peng X and Collings E W 2014 Refinement of Nb₃Sn grain size by the generation of ZrO₂ precipitates in Nb₃Sn wires *Appl. Phys. Lett.* **104** 082602
- [23] Elen J, Van Beijnen C and Van der Klein C 1977 Multifilament V₃Ga and Nb₃Sn superconductors produced by the ECN-technique *IEEE Trans. Magn.* **13** 470–3
- [24] Motowidlo L R and Ozeryansky G M 2008 A new PIT Nb₃Sn conductor for high magnetic field applications *IEEE Trans. Appl. Supercond.* **18** 1001–4
- [25] Motowidlo L R and Ozeryansky G M 2008 A Nb₃Sn conductor via Cu₅Sn₄ PIT process for high field applications *AIP Conf. Proc.* **986** 269–76
- [26] Kramer E J 1973 Scaling laws for flux pinning in hard superconductors *J. Appl. Phys.* **44** 1360–70
- [27] Xu X, Sumption M D and Peng X 2015 Internally oxidized Nb₃Sn strands with fine grain size and high critical current density *Adv. Mater.* **27** 1346–50
- [28] Bhartiya S, Sumption M D, Xuan P, Gregory E, Tomsic M J and Collings E W 2009 Investigation of the effects of low temperature heat treatments on the microstructure and properties of multifilamentary, tube-type Nb₃Sn strands *IEEE Trans. Appl. Supercond.* **19** 2588–92
- [29] Xu X 2017 Fermilab, private communication
- [30] Lee P J, Fischer C M, Naus M T, Squitieri A A and Larbalestier D C 2003 The microstructure and microchemistry of high critical current Nb₃Sn strands manufactured by the bronze, internal-Sn and PIT techniques *IEEE Trans. Appl. Supercond.* **13** 3422–5
- [31] Segal C et al 2016 Evaluation of critical current density and residual resistance ratio limits in powder in tube Nb₃Sn conductors *Supercond. Sci. Technol.* **29** 085003
- [32] Baumgartner T, Eisterer M, Weber H W, Flükiger R, Scheuerlein C and Bottura L 2015 Performance boost in industrial multifilamentary Nb₃Sn wires due to radiation induced pinning centers *Sci. Rep.* **5** 10236
- [33] Xu X, Peng X, Sumption M and Collings E W 2017 Recent progress in application of internal oxidation technique in Nb₃Sn strands *IEEE Trans. Appl. Supercond.* **27** 1–5
- [34] Cooley L D and Lee P J 2001 Shift of the flux-pinning force curve in Nb₃Sn thin films with very fine grain size *IEEE Trans. Appl. Supercond.* **11** 3820–3
- [35] Fischer C, Lee P and Larbalestier D 2002 Irreversibility field and critical current density as a function of heat treatment time and temperature for a pure niobium powder-in-tube Nb₃Sn conductor *Adv. Cryo. Eng.* **48** 1008–15
- [36] Suenaga M, Welch D O, Sabatini R L, Kammerer O F and Okuda S 1986 Superconducting critical temperatures, critical magnetic fields, lattice parameters, and chemical compositions of 'bulk' pure and alloyed Nb₃Sn produced by the bronze process *J. Appl. Phys.* **59** 840
- [37] Farrell H H, Gilmer G H and Suenaga M 1974 Grain boundary diffusion and growth of intermetallic layers: Nb₃Sn *J. Appl. Phys.* **45** 4025–35